Nano Research

Open Access

Research Article

Stem cell-derived biomimetic apoptotic vesicles enhance macrophage efferocytosis via C1qbp to accelerate diabetic wound healing

Le Ding[1,2,3,§], Tingrui Zhang[2,3,§], Yixiao Pan[4,§], Jun Liu[2,3], Jiaye Lu[2,3], Xinyue Zhang[2,3], Tianyou Ma[2,3,5], Donghao Li[2,3], Zhen Cui[2,3], Ying Gao[6], Quangang Zhu[2,3] ✉, Zongguang Tai[2,3] ✉, and Zhongjian Chen[1,2,3] ✉

[1] *Shanghai University, School of Medicine, 99 Shangda Road, Shanghai 200444, China*
[2] *Shanghai Skin Disease Hospital, School of Medicine, Tongji University, 1278 Baode Road, Shanghai 200443, China*
[3] *Shanghai Engineering Research Center of External Chinese Medicine, Shanghai 200443, China*
[4] *Department of Liver Surgery and Liver Transplantation, Renji Hospital, School of Medicine, Shanghai Jiao Tong University, Shanghai 200127, China*
[5] *Department of Pharmacy, Longhua Hospital of Shanghai University of Traditional Chinese Medicine, 725, Wanping South Road, Xuhui District, Shanghai 200032, China*
[6] *Department of Dermatology, The Central Hospital of Wuhan, Tongji Medical College, Huazhong University of Science and Technology, Wuhan 430014, China*
[§] *Le Ding, Tingrui Zhang and Yixiao Pan contributed equally to this work.*

Cite this article: *Nano Research*, **2026**, *19*, 94908650. https://doi.org/10.26599/NR.2026.94908650

ABSTRACT: Chronic diabetic wounds represent a significant therapeutic challenge, characterized by persistent inflammation, impaired angiogenesis, and defective efferocytosis. In this study, we demonstrate that stem cell-derived biomimetic apoptotic vesicles (AVs) are enriched with complement C1q-binding protein (C1qbp), and confirm that C1qbp is a key regulator for macrophage phagocytosis. These AVs potently enhanced macrophage efferocytic activity, promoted polarization from the pro-inflammatory M1 to the anti-inflammatory M2 phenotype, and reduced secretion of the pro-inflammatory cytokines interleukin-1β (IL-1β), IL-6, and tumor necrosis factor-α (TNF-α). Moreover, AVs stimulated angiogenesis and cell migration, thereby initiating a coordinated immune-mediated tissue regenerative program. Delivery of AVs via a GelMA hydrogel (AVs@GelMA) markedly accelerated wound healing in diabetic mice by inhibiting nuclear factor-κB (NF-κB)-driven inflammatory signaling and promoting vascularization and tissue remodeling. Collectively, our findings elucidate a three-phase mechanism of "efferocytosis-immunity-regeneration" and highlight C1qbp-enriched AVs as a promising precision therapeutic strategy for chronic diabetic wounds.

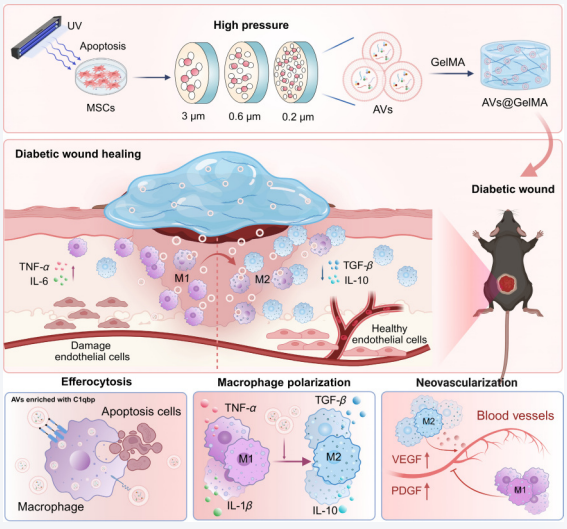

KEYWORDS: apoptotic vesicles, efferocytosis, diabetic wound healing, macrophage polarization, angiogenesis

1 Introduction

The global burden of diabetes mellitus has increased steadily over recent decades, with the number of patients reaching 537 million worldwide [1–3]. Diabetic Foot Ulcer (DFU) is a prevalent and severe complication in patients with diabetes, characterized by persistent wounds on the foot that exhibit poor healing [4, 5]. This condition often necessitates prolonged treatment, considerably diminishes patients' quality of life, and imposes a significant financial burden due to high medical costs [6]. More critically, DFU substantially increases the risk of amputation. For patients who undergo a major amputation, the five-year mortality rate exceeds 70% [7, 8]. Despite the urgent clinical demand for breakthrough therapies to improve wound healing and reduce amputation rates, only a handful of new treatments have achieved FDA approval for efficacy since 1998 [9].

Received: November 28, 2025; **Revised:** March 13, 2026
Accepted: March 18, 2026

✉Address correspondence to Quangang Zhu, qgzhu@126.com; Zongguang Tai, taizongguang@126.com; Zhongjian Chen, aajian818@163.com

Wound healing is a highly coordinated, multistage physiological process encompassing hemostasis, inflammation, proliferation, and tissue remodeling [10]. However, this process is profoundly impaired in diabetic wounds. Aberrant immune responses in DFU trigger persistent and excessive inflammation, impaired angiogenesis, and defective fibroblast-mediated extracellular matrix remodeling, thereby further delaying the healing process [11–13]. The accumulation of apoptotic cells is closely associated with these pathological changes. Normal physiological wound healing relies on macrophage-mediated efferocytosis to clear apoptotic debris and initiate tissue repair [14]. This clearance process depends on the recognition of "eat-me" signals, such as phosphatidylserine, on dying cells [15, 16]. Through successful efferocytosis, macrophages release anti-inflammatory cytokines (including interleukin-10 (IL-10) and transforming growth factor-β (TGF-β)) to resolve local inflammation [17, 18]. In contrast, in diabetes, prolonged hyperglycemia severely impairs this critical efferocytic capacity [17, 19]. Consequently, uncleared apoptotic cells accumulate and undergo secondary necrosis, releasing abundant damage-associated molecular patterns (DAMPs) [20, 21]. This DAMP cascade activates pattern recognition receptors and sustains nuclear factor-κB (NF-κB) signaling, trapping macrophages in a persistent pro-inflammatory (M1) state with continuous secretion of tumor necrosis factor-α (TNF-α) and IL-6 [22, 23]. This vicious cycle blocks their phenotypic transition to the pro-healing (M2) state, thereby inhibiting the secretion of anti-inflammatory cytokines and stalling downstream angiogenesis and extracellular matrix remodeling [24, 25]. Therefore, developing targeted interventions to rescue macrophage efferocytosis is essential to break this chronic inflammatory lock and accelerate diabetic wound healing.

Mesenchymal stem cells (MSCs), with their low immunogenicity and pro-regenerative secretome, are widely studied in wound repair and tissue regeneration [26, 27]. However, the therapeutic benefits of MSCs are not solely dependent on their viability or secretory activity [28]. Rather, apoptosis of transplanted MSCs has emerged as a pivotal step in mediating their immunomodulatory effects [29]. Studies have shown that apoptotic MSCs are rapidly engulfed by phagocytic cells, including alveolar macrophages, monocytes, and neutrophils, which then reprogram their metabolic and inflammatory states to enhance the production of anti-inflammatory cytokines (such as IL-10 and TGF-β) and thereby contribute to disease resolution [30].

In this study, we engineered stem cell-derived biomimetic apoptotic vesicles (AVs) using a reproducible extrusion method. AVs can be efficiently taken up by macrophages. Proteomic analysis identified significant enrichment of complement C1q-binding protein (C1qbp) in AVs, which enhances efferocytosis by facilitating C1q anchoring to apoptotic targets, thereby promoting macrophage clearance and polarization toward the M2 phenotype while reducing pro-inflammatory cytokine secretion. Additionally, AVs improved keratinocyte viability and stimulated angiogenesis. In diabetic mice, AVs delivered via GelMA hydrogel (AVs@GelMA) significantly accelerated wound closure through enhanced efferocytosis-driven macrophage polarization, suppression of NF-κB-mediated inflammation, promotion of angiogenesis, and improved extracellular matrix remodeling. This study establishes a scalable strategy for producing functional AVs and uncovers a sequential therapeutic paradigm of "efferocytosis-immunity-regeneration", highlighting their potential as a precision nanotherapeutic for chronic diabetic wounds.

2 Experimental

2.1 Cell culture and characterization

The murine macrophage cell line RAW264.7, human umbilical vein endothelial cells (HUVECs), Jurkat cells, NIH3T3 fibroblasts, HaCaT keratinocytes, and human placenta-derived mesenchymal stem cells (PMSCs) were purchased from the Chinese Academy of Sciences Cell Bank (Shanghai, China). PMSCs were cultured in Dulbecco's modified Eagle's medium (DMEM) supplemented with 10% fetal bovine serum (FBS) and 1% Penicillin-Streptomycin (P/S) at 37 °C in a 5% CO_2 humidified incubator. Cells from passages 3 to 5 were used for all experiments. Flow cytometry was performed using anti-CD90, anti-CD34, and anti-human leukocyte antigen-DR (HLA-DR) antibodies (ABclonal, China) and anti-CD73 and anti-CD29 antibodies (Invitrogen, USA) to verify the MSC immunophenotype. Analysis was performed on a BD FACSAria II (BD Biosciences, USA) and interpreted with FlowJo software.

2.2 UVB-induced apoptosis and vesicle engineering

To generate AVs, PMSCs were exposed to ultraviolet B (UVB) irradiation (302 nm, 100 mJ/cm^2 total dose) using a UV crosslinker (UVP CL-1000L, Analytik Jena, Germany) for 60 min, followed by incubation for 12 h to complete the apoptosis process. Cells were stained with annexin V-fluorescein isothiocyanate (Annexin V-FITC)/propidium iodide (PI) (Beyotime, China) according to the manufacturer's instructions. Annexin V-FITC/PI dual staining and flow cytometry were used to confirm the efficiency of apoptosis (> 95%). Apoptotic and normal (untreated) cells were then extruded sequentially through 3.0, 0.6, and 0.2 μm polycarbonate membranes (Merck, Germany) using a high-pressure extruder (NanoAble-150, PhD Technology LLC, USA) to generate size-controlled vesicles: AVs and normal vesicles (NVs), respectively.

2.3 Vesicle characterization and stability evaluation

Particle size, polydispersity index (PDI), and zeta potential were measured by dynamic light scattering (DLS) and electrophoretic light scattering (ELS) using a Zetasizer Nano ZS (Malvern Instruments, UK). Vesicle morphology was visualized via transmission electron microscopy (TEM) (HT7800, Hitachi, Japan). Protein concentration was quantified using a bicinchoninic acid (BCA) assay (Beyotime, China), and protein profiles were compared by sodium dodecyl sulfate-polyacrylamide gel electrophoresis (SDS-PAGE) between MSCs and NVs, as well as between apoptotic MSCs and AVs. Gels were stained with Coomassie Brilliant Blue (Beyotime, China). Western blotting was performed to detect cleaved caspase-3 (Cell Signaling Technology, USA) expression in MSCs, apoptotic MSCs, and AVs, confirming the apoptotic nature of AV cargo. To assess vesicle stability, AVs and NVs were stored at 4 and −80 °C for 27 days, and changes in particle size and PDI were monitored over time.

2.4 *In vitro* uptake of NVs and AVs by RAW264.7

To evaluate the uptake of NVs and AVs by RAW264.7 cells *in vitro*, RAW264.7 macrophages were first seeded into culture dishes and incubated with Dio-labeled AVs or NVs (Beyotime, China) for 4 h. After incubation, cells were washed three times with phosphate-buffered saline (PBS) to remove excess, non-internalized vesicles. Subsequently, lysosomes were stained with LysoTracker Red (Beyotime, China) for 40 min, followed by three PBS washes. After

fixation with 4% paraformaldehyde (30 min, room temperature), nuclei were counterstained using 4',6-diamidino-2-phenylindole (DAPI) (Beyotime, China). The uptake and intracellular distribution of vesicles were examined using a laser scanning confocal microscope (LSCM) (Ti2-E + A1R, Nikon, Japan).

2.5 Extraction and culture of BMDMs

Bone marrow-derived macrophages (BMDMs) were prepared from male C57BL/6J mice aged 8–12 weeks. Bone marrow cells were flushed from the femurs and tibias using sterile PBS and treated with red blood cell lysis buffer (Beyotime, China). The cell suspension was centrifuged at 400×*g* for 5 min, and the pelleted cells were resuspended in high-glucose DMEM supplemented with 10% FBS and 20 ng/mL macrophage colony-stimulating factor (M-CSF) (Peprotech, USA). On day 3, half of the medium was replaced, and on day 5, the medium was completely refreshed. Mature BMDMs were harvested on day 7 and identified by flow cytometry using F4/80 and CD11b (Invitrogen, USA) surface markers.

2.6 Induction and labeling of apoptotic Jurkat cells

Jurkat cells were exposed to UV irradiation at a dose of 150 mJ/cm^2 using a UV crosslinker, followed by incubation at 37 °C in 5% CO_2 for 4 h to induce apoptosis. Cells were subsequently labeled with PI to identify apoptotic populations.

2.7 Phagocytosis assay and analysis

Western blotting was performed to detect C1qbp (Proteintech, USA) expression in AVs and NVs. Mature BMDMs were divided into five experimental groups: Control, NVs, AVs, Anti-C1q, and Anti-C1q+AVs. For pretreatment, BMDMs were incubated with NVs or AVs for 24 h, or with anti-C1q antibody (1 ng/mL, Selleck, USA) for 1 h prior to apoptotic cell addition. Apoptotic Jurkat cells labeled with PI were then co-incubated with BMDMs at a ratio of 1:5 for 4 h. For confocal imaging, BMDMs were additionally labeled with Calcein AM (Beyotime, China) to visualize cell boundaries, followed by observation of efferocytosis under a laser scanning confocal microscope. For flow cytometric analysis, BMDMs were instead identified by surface staining with CD11b and F4/80 (Invitrogen, USA), and PI signals were used to quantify internalized apoptotic cells.

2.8 Cell viability

Cell viability of HaCaT keratinocytes was determined by the cell counting kit-8 (CCK-8) assay (ABclonal, China). Following seeding into 96-well plates, cells were incubated with AVs or NVs at concentrations of 10–150 μg/mL. After 24 h of incubation, CCK-8 working solution was added to each well and incubated for the recommended period. The absorbance was then measured at 450 nm using a microplate reader to determine cell viability and identify the optimal treatment concentration.

2.9 Migration assays

A scratch wound assay was performed to evaluate the effect of vesicles on cell migration. Cells were seeded in 6-well plates and cultured until they formed a confluent monolayer (≥ 90% confluency). A linear scratch was created using a sterile 200 μL pipette tip. Detached cells were gently removed by washing with PBS. Cells were then incubated in medium containing 30, 50, or 70 μg/mL of either AVs or NVs. Images of the wound area were captured at 0, 24, and 48 h. To enhance visualization of cell morphology and migration front, cells were stained with Calcein-AM (Beyotime, China) prior to imaging.

To examine migratory capacity, cells suspended in serum-free medium were seeded in the upper compartment of transwell inserts (8 μm pore polycarbonate membranes, Corning, USA). The lower chamber was filled with medium containing 5% FBS as a chemoattractant, along with AVs or NVs at the indicated concentrations (30, 50, and 70 μg/mL). After 24 h of incubation, cells remaining on the upper membrane surface were carefully wiped away with a cotton swab. Cells that had traversed to the lower side were fixed in 4% paraformaldehyde for 30 min and subsequently stained with crystal violet for 30 min. Excess dye was removed by rinsing with PBS, and images were captured using an optical microscope.

2.10 Live/dead cell staining assay

HUVECs were treated for 24 h and then subjected to live/dead staining using a Cell Viability Assay Kit (Beyotime, China) following the manufacturer's instructions. Cells were first rinsed with PBS, then incubated with Calcein-AM and PI at 37 °C for 30 min in darkness. Live cells were stained with Calcein-AM for green fluorescence, and dead cells were stained with PI for red. After staining, PBS washing was performed, and the samples were observed under a fluorescence microscope.

2.11 Endothelial cell angiogenesis assays

HUVECs were seeded onto growth factor-reduced Matrigel-coated 48-well plates and treated with NVs or AVs (70 μg/mL) to evaluate their direct pro-angiogenic effects. To further investigate whether AVs initiate angiogenesis via macrophage immunomodulation, a macrophage-conditioned medium (CM) assay was simultaneously performed. RAW264.7 macrophages were pre-stimulated with lipopolysaccharide (LPS) (1 μg/mL) for 24 h and then treated with PBS, NVs or AVs (70 μg/mL) for 24 h. The cells were thoroughly washed with PBS and cultured in fresh endothelial basal medium for another 24 h. The supernatants were collected, centrifuged to remove debris, and applied to HUVECs seeded on Matrigel-coated plates. After 6 h of incubation, cells from all treatments were stained with Calcein-AM at 37 °C for 20 min in the dark. After washing with PBS, tube formation was imaged using a fluorescence microscope. Quantification of total tube length and the number of branch points was performed using ImageJ software.

2.12 Flow cytometry analysis

RAW264.7 macrophages were pre-stimulated with LPS (1 μg/mL) for 24 h to induce an M1 phenotype and then treated with AVs, NVs (70 μg/mL), or PBS for 24 h. After treatment, cells were collected, washed, and stained with anti-CD86 and anti-CD206 antibodies (Invitrogen, USA) for 30 min at 4 °C in the dark. Samples were analyzed using a flow cytometer and the data were processed with FlowJo software.

For immunofluorescence staining, RAW264.7 cells were fixed in 4% paraformaldehyde (PFA), permeabilized with 1% Triton X-100 for 10 min, blocked with 1% bovine serum albumin (BSA) for 1 h at room temperature, and incubated overnight at 4 °C with the following primary antibodies: anti-CD206 and anti-CD86 (Cell Signaling Technology, USA). Nuclei were counterstained with DAPI, and images were captured using LSCM to visualize macrophage polarization.

2.13 Quantitative real-time PCR (RT-qPCR)

To prepare samples for gene expression analysis, cells and tissues were processed as follows. For the macrophage polarization assay, RAW264.7 cells were pre-stimulated with LPS (1 μg/mL) for 24 h and incubated with NVs or AVs for an additional 24 h. To validate the C1qbp-dependent mechanism, both LPS-stimulated RAW264.7 cells and BMDMs were pre-treated with an anti-C1qbp antibody (1 ng/mL, Thermo Fisher Scientific, USA) for 1 h prior to a 24 h AVs co-incubation. In all *in vitro* assays, unstimulated cells and LPS-only treated cells were included as baseline controls. For *in vivo* evaluations, day 7 wound tissues were mechanically homogenized in lysis buffer using a tissue grinder to ensure complete cell disruption.

Total RNA from the aforementioned cultured cells and tissue homogenates was isolated using an RNA extraction kit (Vazyme, China) according to the manufacturer's protocol. Complementary DNA (cDNA) was synthesized using a reverse transcription kit (Vazyme, China). Quantitative real-time PCR was performed using the LightCycler® 480 II Real-Time PCR System (Roche, Switzerland) with gene-specific primers. Gene expression was analyzed using the $2^{-\Delta\Delta CT}$ approach, normalized to glyceraldehyde-3-phosphate dehydrogenase (GAPDH). Primer details can be found in Table S1 in the Electronic Supplementary Material (ESM).

2.14 Enzyme-linked immunosorbent assay (ELISA)

The concentrations of cytokines in the culture supernatants were measured using enzyme-linked immunosorbent assay (ELISA) kits (ABclonal, China) according to the manufacturer's instructions. The analyzed cytokines included pro-inflammatory markers (TNF-α, interleukin-1β (IL-1β), IL-6), anti-inflammatory cytokines (IL-10, TGF-β), and growth factors (vascular endothelial growth factor (VEGF), platelet-derived growth factor (PDGF), and fibroblast growth factor 2 (FGF2)).

2.15 Nitric oxide (NO) production assay

To evaluate the inhibitory effect of vesicles on NO production, RAW264.7 macrophages were pre-stimulated with LPS (1 μg/mL) for 24 h to induce an inflammatory state, followed by treatment with NVs or AVs (70 μg/mL) for another 24 h. The accumulation of NO in the culture supernatants was measured using a Griess Reagent System (Beyotime, China) according to the manufacturer's instructions. The absorbance was determined at 540 nm using a microplate reader.

2.16 Hydrogel preparation and characterization

To compare the *in vivo* functions of NVs and AVs, 100 μg of each vesicle type was mixed with 5% gelatin methacryloyl (GelMA) hydrogel solution (Engineering For Life, China) to form NV-loaded GelMA (NVs@GelMA) and AVs@GelMA composites. GelMA prepolymer solution was prepared and mixed with 0.5% (w/v) photoinitiator, and the vesicle-loaded mixtures were subjected to UV irradiation for 10–30 s to achieve *in situ* crosslinking. The microstructure of the hydrogels was observed by scanning electron microscopy (SEM) using a ZEISS Sigma 300 system (Carl Zeiss, Germany). Briefly, hydrogels were freeze-dried at −80 °C to remove moisture and then sputter-coated with a thin layer of gold to enhance conductivity before imaging. SEM analysis was performed for plain GelMA hydrogels as well as vesicle-loaded hydrogels (NVs@GelMA and AVs@GelMA) to compare their internal pore structures.

2.17 *In vitro* vesicle release assay

To assess vesicle release kinetics, 1 mL of AVs@GelMA or NVs@GelMA sample was immersed in 1 mL PBS and incubated. At predetermined time points, the supernatant was collected and replaced with fresh PBS. The released protein content was quantified using the BCA assay, and the cumulative release profile was plotted using GraphPad Prism software.

2.18 *In vivo* diabetic wound healing assay

Male C57BL/6 mice (6–8 weeks old) were obtained from SPF Biotechnology Co., Ltd. (Suzhou, China) and kept in a specific pathogen-free (SPF) environment. All animal experiments were conducted in strict accordance with the Guidelines for the Use of Laboratory Animals and were approved by the Ethics Committee of Shanghai Skin Disease Hospital, Shanghai, China (approval ID: 2021-91). To induce diabetes, mice (except those in the Control group) received a single intraperitoneal injection of Streptozotocin (STZ) (150 mg/kg, Macklin, China) freshly prepared in 0.1 M citrate buffer (pH 4.5). On day 7 post-injection, mice with fasting blood glucose levels consistently above 16.7 mmol/L were considered successfully modeled and included in subsequent experiments.

Mice were randomly divided into six groups (n = 5 mice per group): Control (non-diabetic), and five diabetic groups including PBS, GelMA, AVs, NVs@GelMA and AVs@GelMA. On day 7 after STZ injection, full-thickness excisional wounds (10 mm in diameter) were created on the dorsal skin under anesthesia. Local treatments were performed on days 0, 3, 7, and 10 post-wounding. For each treatment, 100 μL of sample was topically applied to the wound, containing 100 μg of vesicles when applicable. In the GelMA-related groups, the hydrogel formulations were applied to the wound surface and crosslinked *in situ* using UV irradiation to form a stable hydrogel dressing.

Wound closure was documented by digital photography on days 0, 3, 7, 10, and 14. The wound area was quantified using ImageJ software. Wound healing rate was calculated using the equation (Eq. (1)):

$$\text{Wound closure rate}\ (\%) = \frac{\text{Area}_0 - \text{Area}_n}{\text{Area}_0} \times 100\% \quad (1)$$

where Area_0 is the initial wound area and Area_n is the wound area at each time point.

2.19 Histological and immunohistochemical analyses

On days 3 and 7 post-wounding, wound tissues were collected to assess early inflammatory responses and cellular apoptosis. Samples were fixed in 4% paraformaldehyde, embedded in paraffin, and sectioned at 5 μm thickness. Immunohistochemistry (IHC) staining was performed to detect IL-10, TNF-α, and phosphorylated p65 (p-p65), markers associated with anti-inflammatory signaling, pro-inflammatory cytokines, and NF-κB pathway activation, respectively. In parallel, immunofluorescence staining was carried out for CD86 and CD206 to evaluate macrophage polarization, and for apoptosis-related markers including terminal deoxynucleotidyl transferase dUTP nick end labeling (TUNEL) (evaluated on both days 3 and 7) and cleaved caspase-3. These analyses allowed for the assessment of apoptotic cell populations in the wound bed.

To further evaluate tissue regeneration and remodeling, additional wound samples were harvested on day 14 post-wounding. Histological staining, including hematoxylin and eosin

(H&E) and Masson's trichrome, was performed to assess epithelialization and collagen deposition, respectively. Immunofluorescence staining was carried out for CD31 (a marker of endothelial cells and angiogenesis), and α-smooth muscle actin (α-SMA) (indicative of myofibroblast activation).

H&E, Masson's trichrome, and IHC stained sections were imaged using a bright-field microscope. Immunofluorescence sections were observed and imaged using a laser scanning confocal microscope. Quantitative image analysis was performed using ImageJ software by measuring the percentage of positive staining area and counting the number of marker-positive cells within the wound tissue.

2.20 Proteomic and transcriptomic analysis

For proteomic analysis, AVs and NVs were prepared by sequential extrusion through polycarbonate membranes. Two experimental groups (AVs and NVs) were established, and each group included three independent biological replicates. The vesicle samples were sent to Shanghai Majorbio Bio-Pharm Technology Co., Ltd. (Shanghai, China) for proteomic sequencing.

For transcriptomic analysis, full-thickness wound skin tissues were collected from diabetic mice at day 7 after treatment. Two experimental groups were included: AVs@GelMA and PBS-treated diabetic wounds as control. Each group contained three biological replicates. The tissue samples were promptly snap-frozen in liquid nitrogen and subjected to RNA sequencing by Shanghai Majorbio Bio-Pharm Technology Co., Ltd.

2.21 Statistical analysis

Data are expressed as the mean ± standard deviation (SD). All results were statistically analyzed and graphically presented using GraphPad Prism 9.0 (GraphPad Software, USA). Student's *t*-test was used to analyze differences between groups, while one-way analysis of variance (ANOVA) was applied for comparisons among three or more groups. All experiments were independently repeated at least three times. Statistical significance was set at $P < 0.05$.

3 Results and discussion

3.1 Construction and characterization of stem cell-derived AVs

To ensure biological consistency and functional relevance of the vesicle source, MSCs were first subjected to phenotypic characterization. Flow cytometric analysis revealed high expression of CD73, CD90, and CD29, with minimal expression of CD34 and HLA-DR, consistent with the classical MSC phenotype (Fig. S1(a) in the ESM). This provided a reliable cellular foundation for subsequent vesicle preparation. Apoptosis was induced in MSCs by UVB irradiation. Morphological changes were time-dependent: at 15 min, cell shrinkage was evident; by 30 min, membrane blebbing emerged; at 45 min, most cells displayed typical apoptotic morphology; and by 60 min, apoptosis was nearly complete (Fig. S1(b) in the ESM). Annexin V-FITC/PI double staining further confirmed that UVB exposure for 60 min resulted in a total apoptosis rate of 96.8% (Fig. S1(c) in the ESM). Therefore, apoptotic MSCs obtained under this condition were used as the source for AV preparation.

To overcome the low yield and high heterogeneity of natural apoptotic bodies, we engineered uniform nanovesicles via mechanical extrusion of these apoptotic MSCs. These extruded AVs are highly biomimetic, preserving the intact lipid bilayer and functional cargo of natural apoptotic cells. DLS analysis showed that the average diameters of AVs and NVs were 186.3 and 182.6 nm, respectively (Figs. 1(a) and 1(b)), indicating good dispersion and size uniformity. Stability tests demonstrated that both vesicle types remained largely stable after six days of storage at 4 or −80 °C, with only slight increases in particle size and PDI (Figs. 1(c)–1(f)). Notably, vesicles preserved at −80 °C exhibited superior stability. TEM revealed that both AVs and NVs possessed a typical phospholipid bilayer structure, appearing spherical with well-defined contours (Fig. 1(g)). These features resembled those of other membrane-derived vesicles such as exosomes, supporting their intrinsic membranous nature. Zeta potential analysis indicated that both vesicle types were negatively charged, although AVs displayed lower surface potential, suggesting alterations in their membrane composition (Fig. S2 in the ESM). SDS-PAGE analysis showed a high degree of similarity between AVs and their parental apoptotic MSCs (apoMSCs) in protein profiles, while NVs closely resembled normal MSCs (Fig. 1(h)). Western blotting further confirmed significantly elevated expression of cleaved caspase-3 in apoMSCs and AVs, whereas this apoptotic marker was nearly absent in normal MSCs (Fig. 1(i)), indicating that AVs retained apoptosis-associated molecular components. To evaluate uptake efficiency and intracellular localization in macrophages, AVs and NVs were labeled with Dio and co-incubated with RAW264.7 macrophages pre-stained with LysoTracker. Confocal laser scanning microscopy (CLSM) revealed that both AVs and NVs were efficiently taken up by macrophages within 4 h and subsequently co-localized with lysosomes, confirming their successful delivery into phagolysosomes (Fig. 1(j)). Notably, the overall fluorescence intensity of AVs in cells was higher than that of NVs, suggesting that AVs may exhibit stronger macrophage targeting and endocytosis efficiency.

In summary, we successfully generated AVs derived from MSCs with well-defined origin, stable composition, apoptotic characteristics, and pronounced macrophage-targeting capacity, together with a corresponding AV control system. These vesicles provide a standardized and reproducible platform for subsequent functional investigations both *in vitro* and *in vivo*.

3.2 *In vitro* pro-regenerative effects of AVs

To further investigate their biological activity and determine an appropriate working concentration, we performed systematic *in vitro* functional assays using multiple cell types relevant to wound repair. First, HaCaT keratinocytes were treated with different concentrations of AVs or NVs, and cell viability was assessed using the CCK-8 assay. Both vesicle types promoted cell proliferation within a certain concentration range (Figs. S3(a) and S3(b) in the ESM), although AVs displayed a stronger effect. Notably, at 70 μg/mL, AVs nearly doubled the proliferation rate compared with the control and exceeded the effect of NVs at the same concentration. Meanwhile, no reduction in cell viability was observed across the tested concentration range, suggesting that both vesicle formulations were well tolerated by HaCaT cells *in vitro*, which is consistent with the generally favorable cytocompatibility reported for biomimetic vesicle systems [31, 32]. Together, these findings provided initial evidence of the superior bioactivity of AVs.

We next examined the effect of AVs on cell migration. Scratch wound assays in NIH3T3 fibroblasts demonstrated that treatment with AVs at 30, 50, and 70 μg/mL significantly increased wound

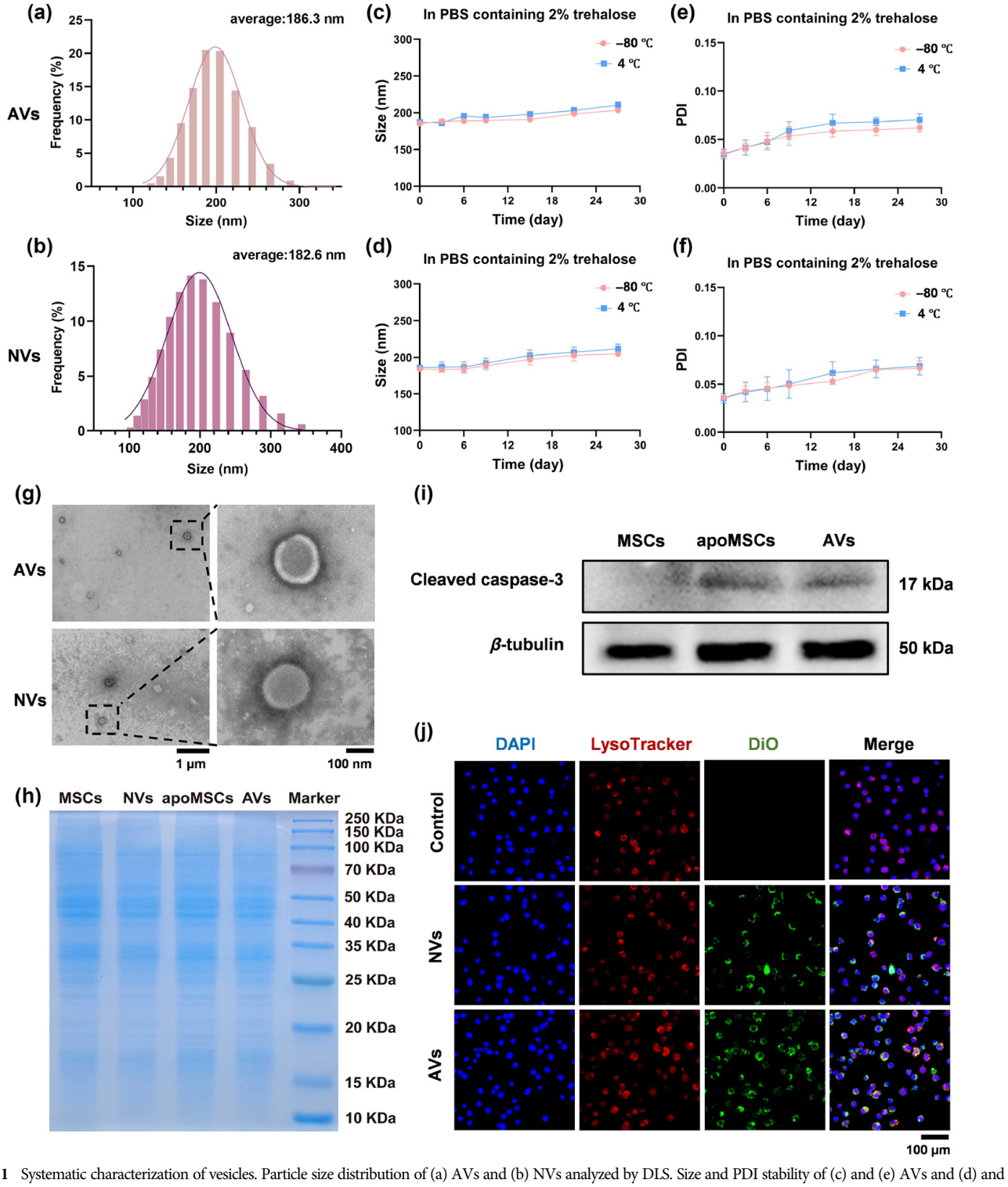

Figure 1 Systematic characterization of vesicles. Particle size distribution of (a) AVs and (b) NVs analyzed by DLS. Size and PDI stability of (c) and (e) AVs and (d) and (f) NVs after 27 days of storage at −80 or 4 °C (n = 3). (g) TEM images of AVs and NVs. (h) SDS-PAGE gel electrophoresis showing protein profiles of MSCs, NVs, apoMSCs, and AVs. (i) Western blot analysis of cleaved caspase-3 expression in AVs compared with MSCs and apoMSCs. (j) Confocal images showing cellular uptake of DiO-labeled AVs and NVs by RAW264.7 cells; lysosomes were labeled with LysoTracker and nuclei with DAPI.

closure at both 24 and 48 h compared with controls, with the most pronounced effect observed at 70 μg/mL (Figs. S4(a) and S4(b) in the ESM). Transwell assays further confirmed this result, showing that AVs increased the number of migrating fibroblasts in a concentration-dependent manner, again with the strongest effect at 70 μg/mL (Figs. S5(a) and S5(c) in the ESM). These results demonstrate that AVs not only accelerate cell lateral migration but also significantly enhance longitudinal chemotactic migration capacity.

A similar enhancement of migration was observed in HUVECs, where AV treatment significantly promoted endothelial cell motility (Figs. S5(b) and S5(d) in the ESM), suggesting a broad pro-

migratory effect across different cell types. Since macrophage polarization is a critical determinant of the wound healing microenvironment, we also investigated the impact of AVs on macrophage phenotype. RAW264.7 macrophages (M0 state) were treated with AVs, and expression of the M2 marker CD206 was analyzed. Flow cytometry revealed a dose-dependent increase in CD206-positive cells, with the proportion rising from 1.5% in the control to 25.6% at 70 μg/mL (Figs. S6(a) and S6(b) in the ESM). This demonstrated that AVs effectively induced macrophage polarization toward the pro-repair M2 phenotype. Collectively, AVs enhanced proliferation, migration, and macrophage polarization in wound healing-related cells, with the strongest biological activity observed at 70 μg/mL. Therefore, this concentration was selected for subsequent *in vitro* experiments.

Given the pronounced pro-migratory activity of AVs, we next evaluated their potential role in regulating angiogenic behaviors of endothelial cells. In HUVECs, scratch assays showed that AV treatment markedly accelerated migration in a clear dose-dependent manner (Figs. 2(a) and 2(b)). Consistent with this trend, live/dead staining further revealed a significantly higher density of live cells in AV-treated HUVECs than those treated with NVs (Figs. 2(c) and 2(d)), indicating a stronger ability to activate endothelial repair processes. Transwell assays confirmed the superior pro-migratory effect of AVs, as evidenced by a significantly greater number of transmigrated cells compared with NV treatment (Figs. 2(e) and 2(f)). Furthermore, in a fibroblast model (NIH3T3), AVs also exhibited a more pronounced pro-migration effect (Figs. S7(a) and S7(b) in the ESM), indicating that their migratory-promoting action is not limited to endothelial cells but may exert regulatory functions across multiple cell types. On this basis, to further substantiate the pro-angiogenic potential of AVs, we performed a Matrigel-based tube formation assay. AV treatment induced HUVECs to form denser and more structurally coherent capillary-like networks (Fig. 2(g)). Quantification showed superiority over NVs in multiple metrics, including total tube length, node number, and branch number (Figs. 2(h) and 2(i)), indicating a stronger inductive capacity during vascular reconstruction. ELISA demonstrated significantly higher secretion of key pro-angiogenic factors, including VEGF, PDGF, and FGF2, in the AV group than in the NV group (Figs. 2(j)–2(l)). This pattern was corroborated at the transcriptional level by qPCR (Fig. S8 in the ESM), further supporting a critical regulatory role of AVs in remodeling the angiogenic microenvironment.

In summary, AVs promoted angiogenesis by enhancing the proliferation and migration of endothelial cells and fibroblasts, while simultaneously upregulating the expression of pro-angiogenic factors, thereby facilitating the formation of vascular-like structures.

3.3 AVs promote efferocytosis

During apoptosis, the activation of specific signaling cascades drives cellular metabolic reprogramming, culminating in the release of AVs enriched with distinct functional cargo. To elucidate the molecular signatures of these vesicles, we performed a comprehensive comparative proteomic analysis between AVs and NVs. Principal component analysis (PCA) revealed a clear distinction between the two groups along PC1 (63.5%) and PC2 (12.5%) (Fig. S9(a) in the ESM). Differential expression analysis identified 280 upregulated and 238 downregulated proteins in AVs (Fig. S9(b) in the ESM) and global hierarchical clustering further confirmed this substantial divergence (Fig. S9(c) in the ESM). A targeted analysis of these differentially expressed proteins revealed that AVs were highly enriched in several critical regulators, including C1qbp, programmed cell death 6-interacting protein (Pdcd6ip, also known as ALIX), apoptosis-inducing factor mitochondria-associated 1 (Aifm1), vacuolar protein sorting-associated protein 45 (Vps45), and sorting nexin-1/2 (Snx1/2) (Fig. S9(d) in the ESM). These proteins mediate apoptotic signaling, target recognition, and phagolysosome maturation, forming the core network for efficient efferocytosis [33–36]. Notably, C1qbp anchors the complement protein C1q, which significantly amplifies apoptotic cell clearance by phagocytes [37, 38]. Our proteomic data demonstrated a more than twofold increase in C1qbp abundance within AVs (Fig. S9(e) in the ESM), which was definitively confirmed by Western blotting (Fig. S9(f) in the ESM).

Together with the previous observation of higher uptake efficiency, the proteomic enrichment of C1qbp suggested that AVs might actively promote efferocytosis by enhancing macrophage recognition. To verify this, we first quantitatively evaluated the macrophage engulfment of apoptotic cells using flow cytometry. The results demonstrated that AV treatment significantly increased the efferocytic efficiency of macrophages compared to the control and NV groups. However, anti-C1q or applying combined treatment (AVs + anti-C1q) effectively abolished this enhancement (Figs. 3(a) and 3(b)). Confocal imaging visually corroborated these findings, revealing abundant intracellular phagocytic signals in the AV group, which were markedly reduced under C1q blockade (Fig. 3(c)). These findings suggest a mechanism where C1qbp on AVs anchors soluble C1q to engage corresponding macrophage receptors, thereby driving targeted engulfment (Fig. 3(d)). To validate this receptor-level activation, we assessed classical TAM efferocytosis receptors (*Mertk*, *Axl*, and *Tyro3*). AV treatment significantly upregulated their mRNA levels in BMDMs, whereas specific blockade of vesicular C1qbp (AVs + anti-C1qbp) profoundly reversed this activation (Fig. 3(e)). Defective efferocytosis causes apoptotic cell accumulation and exacerbated inflammation, ultimately leading to chronic wounds. Furthermore, excessive apoptotic cell retention impairs macrophage clearance via negative feedback, driving their pro-inflammatory polarization [39]. Efferocytosis is inherently coupled with the resolution of inflammation, a process largely driven by the suppression of the NF-κB signaling pathway [14, 18]. To determine whether AV-enhanced engulfment triggers this downstream anti-inflammatory response, we evaluated the cytokine profiles in LPS-stimulated macrophages. As expected, AVs robustly downregulated the expression of pro-inflammatory cytokines (*TNF-α*, *IL-6*, and *IL-1β*) at both the transcriptional (Fig. 3(f)) and translational secretion levels (Fig. S10 in the ESM). Crucially, pre-treatment with the anti-C1qbp antibody entirely counteracted this anti-inflammatory effect. Collectively, these results elucidate that AVs not only enhance efferocytosis but also actively mitigate inflammatory responses specifically via the C1qbp/C1q axis.

3.4 AVs balance macrophage phenotypes and modulate inflammatory cytokine expression

In the chronic wound microenvironment, persistent inflammation and imbalanced macrophage polarization are primary drivers of delayed repair. Having established that AVs suppress early inflammatory signaling, we investigated their capacity to orchestrate a comprehensive phenotypic transition toward a pro-repair state. As expected, LPS stimulation markedly upregulated the M1 marker

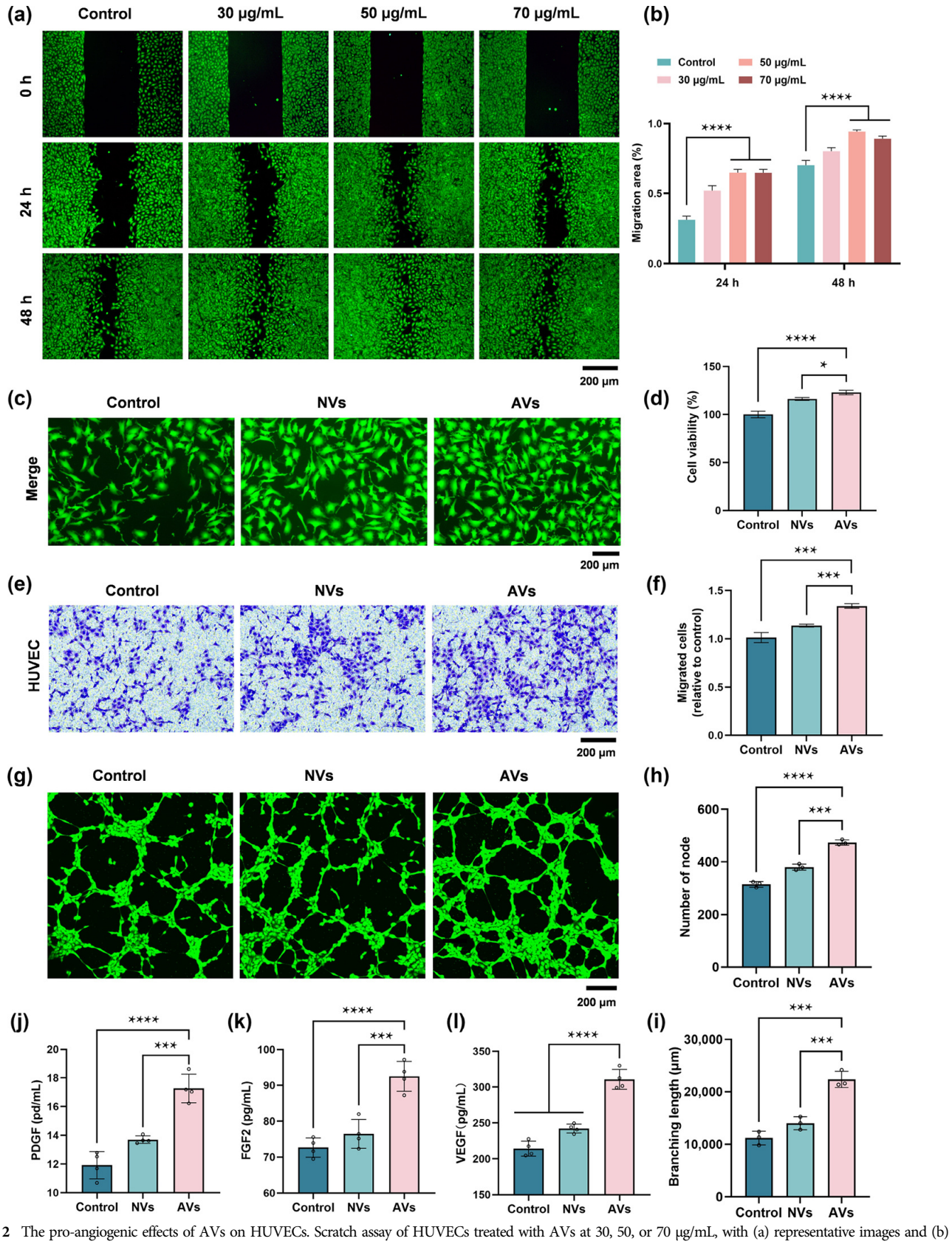

Figure 2 The pro-angiogenic effects of AVs on HUVECs. Scratch assay of HUVECs treated with AVs at 30, 50, or 70 μg/mL, with (a) representative images and (b) quantification of wound closure (%). (c) Live/dead fluorescence staining of HUVECs under different treatments and (d) quantitative analysis of cell viability. Transwell assay evaluating the effect of AVs and NVs on HUVEC migration, with (e) representative images and (f) quantification of transmigrated cells. (g) Matrigel tube formation assay of HUVECs under different treatments and quantitative analysis of (h) node number and (i) branch length of formed vascular-like networks. ELISA analysis of angiogenic factor secretion in HUVECs, including (j) PDGF, (k) FGF2, and (l) VEGF (n = 4). Data are presented as mean ± SD (n = 3, unless otherwise specified). *P < 0.05; **P < 0.01; ***P < 0.001; ****P < 0.0001.

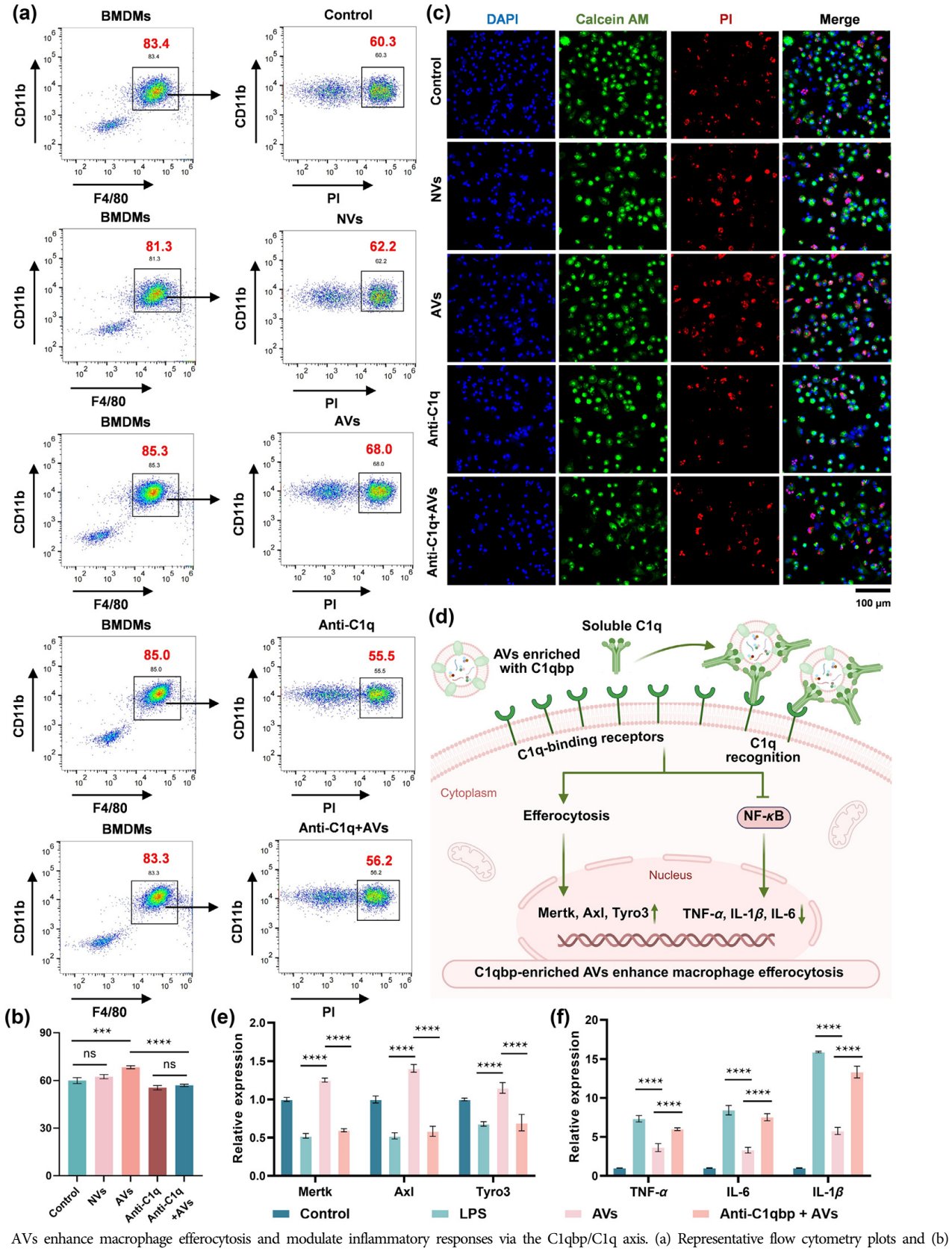

Figure 3 AVs enhance macrophage efferocytosis and modulate inflammatory responses via the C1qbp/C1q axis. (a) Representative flow cytometry plots and (b) quantitative analysis evaluating the efferocytosis of apoptotic cell (PI^+) engulfment by BMDMs ($F4/80^+CD11b^+$). (c) Representative immunofluorescence images demonstrating the engulfment of apoptotic cells (PI, red) by BMDMs (Calcein AM, green). Nuclei were stained with DAPI (blue). (d) Schematic illustration depicting the molecular mechanism: C1qbp-enriched AVs anchor soluble C1q to bind corresponding macrophage receptors, thereby enhancing efferocytosis and downregulating NF-κB-mediated inflammatory signaling. (e) RT-qPCR analysis of efferocytosis-related receptors (*Mertk*, *Axl*, *Tyro3*) in BMDMs. (f) RT-qPCR analysis of pro-inflammatory cytokines (*TNF-α*, *IL-6*, *IL-1β*) in RAW264.7 cells. Data are presented as mean ± SD ($n = 3$). $^*P < 0.05$; $^{**}P < 0.01$; $^{***}P < 0.001$; $^{****}P < 0.0001$.

CD86 (Fig. 4(a)). However, subsequent intervention with AVs significantly reversed this trend, drastically reducing the proportion of CD86-positive cells while concurrently upregulating the M2 marker CD206. Notably, AVs exhibited a substantially more potent regulatory effect in driving this M2 polarization compared to NVs (Figs. 4(a) and 4(b)). This phenotypic transition was also confirmed by immunofluorescence staining. Following AV treatment, CD206 fluorescence intensity in macrophages was enhanced, whereas CD86 fluorescence was relatively reduced, indicating a shift towards the anti-inflammatory M2 phenotype. The effect of NVs was weaker in comparison (Fig. 4(d)). These results were consistent with flow cytometry, suggesting that AVs have a superior capacity to reprogram macrophage phenotypes. To further investigate whether phenotypic switching was accompanied by changes in cytokine expression, we measured the secretion of inflammation-related cytokines. ELISA results showed that AVs significantly suppressed the secretion of pro-inflammatory cytokines TNF-α, IL-1β, and IL-6, while enhancing the secretion of anti-inflammatory cytokines IL-10 and TGF-β (Fig. 4(e)). qPCR further confirmed that AV treatment effectively downregulated the transcription of M1-associated genes *TNF-α*, *IL-6*, and *IL-1β* (Fig. S11(a) in the ESM), while significantly upregulating mRNA expression of M2 markers including *Arg-1*, *IL-10*, and *TGF-β* (Fig. S11(b) in the ESM). In addition, NO assays showed that AVs markedly reduced NO production in LPS-stimulated RAW264.7 cells (Fig. S12 in the ESM), further supporting their ability to suppress inflammatory activation. Although NVs also exerted a certain inhibitory effect, their efficacy was clearly weaker than that of AVs. Crucially, to verify whether this AV-driven macrophage reprogramming translates into functional tissue repair benefits, we evaluated the pro-angiogenic capacity of the macrophage CM. HUVECs cultured in AV-treated macrophage CM exhibited significantly enhanced tube formation abilities compared to those in the NV-CM and Control-CM groups, as evidenced by a profound increase in both the number of nodes and total branching length (Figs. 4(f) and 4(g)). Collectively, these findings demonstrate that AV-mediated efferocytosis robustly suppresses M1 polarization and pro-inflammatory cytokine secretion, driving a decisive phenotypic shift toward an anti-inflammatory M2 state (Fig. 4(c)). Integrating these functional outcomes with our proteomic data, we propose that AVs establish a permissive foundation for angiogenesis and tissue repair by enhancing apoptotic clearance and resolving the local inflammatory milieu. Ultimately, this orchestrates a three-phase synergistic mechanism of "efferocytosis-immunity-regeneration", highlighting the profound therapeutic potential of AVs in chronic wound healing.

3.5 *In vivo* evaluation of AVs@GelMA hydrogels in diabetic wound healing

To achieve stable and sustained local release of AVs at wound sites, we constructed a controlled delivery system by incorporating AVs into biocompatible GelMA hydrogels (Fig. 5(b)). Scanning electron microscopy revealed that all GelMA hydrogels displayed a characteristic porous network structure, which is favourable for vesicle loading and release (Fig. S13(a) in the ESM). Release profiles demonstrated that both NVs@GelMA and AVs@GelMA achieved rapid and sustained vesicle release during the first four days (Figs. S13(c) and S13(d) in the ESM). The AVs@GelMA hydrogel solution exhibited fluidity when the vial was tilted, but underwent a rapid sol-gel transition upon UV exposure, after which no flow was observed. Furthermore, AVs@GelMA hydrogels could be easily injected using a prepared syringe (Fig. S13(b) in the ESM).

To validate the therapeutic potential of AVs *in vivo*, we established a full-thickness skin defect model in STZ-induced diabetic mice (Fig. 5(a)). Diabetes was induced by intraperitoneal injection of STZ, and animals with stable blood glucose levels ≥ 16.7 mmol/L were included (Fig. S14(a) in the ESM). Subsequently, circular full-thickness skin wounds with a diameter of 10 mm were created on the dorsal surface. As shown in Fig. 5(c) and Fig. S14(b) in the ESM, the Control group (healthy mice without diabetes) exhibited the fastest wound closure and complete healing throughout the experiment, reflecting normal physiological repair capacity. In contrast, wounds in the PBS and GelMA groups closed slowly, with insufficient collagen deposition and neovascularization, indicating the limited reparative potential of GelMA alone. The AVs-treated group was characterized by accelerated edge contraction and granulation tissue coverage. Importantly, the AVs@GelMA group consistently demonstrated the most stable and pronounced wound closure at all-time points, significantly outperforming the NVs@GelMA group and reaching healing levels approaching those of the healthy Control group.

H&E staining (Fig. 5(d)) revealed that while AV treatment alone improved epithelialization and reduced inflammatory infiltration relative to the PBS and GelMA groups, the AVs@GelMA hydrogel achieved the most superior structural restoration. This group exhibited a continuous, well-stratified epithelium, and effectively minimized inflammatory cell infiltration (Fig. 5(f)). Furthermore, Masson's trichrome staining (Fig. 5(e)) highlighted robust extracellular matrix remodeling. Tissues treated with AVs@GelMA displayed highly organized, dense, and uniformly compacted collagen networks, resulting in a significantly greater collagen deposition area compared to the NVs@GelMA group (Fig. 5(g)). Crucially, beyond matrix deposition, the AVs@GelMA treatment profoundly augmented the regeneration of skin appendages, as evidenced by a significantly higher number of newly formed hair follicles (Fig. 5(h)). Taken together, these histological findings underscore the exceptional efficacy of AVs@GelMA in orchestrating comprehensive and high-quality diabetic wound healing.

3.6 AVs@GelMA orchestrate an *in vivo* "efferocytosis-immunity-regeneration" cascade

To elucidate the *in vivo* mechanisms of AVs@GelMA, we evaluated the wound microenvironment across distinct healing phases (days 3, 7, and 14). Rather than merely acting at a single stage, AVs@GelMA orchestrates a sequential repair program, where early apoptotic clearance actively drives subsequent immune resolution and vascular regeneration. At the early inflammatory stage (day 3), TUNEL staining (Fig. 6(a)) revealed extensive apoptotic accumulation in the PBS and GelMA groups. Conversely, AVs@GelMA treatment effectively accelerated this clearance, achieving a significantly lower apoptotic cell density compared to the NVs@GelMA group (Fig. 6(d)). This confirms that localized AV delivery robustly promotes *in vivo* efferocytosis, rapidly clearing early inflammatory triggers from the wound bed. Driven by this efficient early clearance, AVs@GelMA successfully reprogrammed the macrophage phenotype to resolve persistent inflammation by day 7. Immunofluorescence for CD206 (M2) and CD86 (M1) (Fig. 6(b)) demonstrated that while NVs@GelMA induced partial M2 polarization, AVs@GelMA consistently

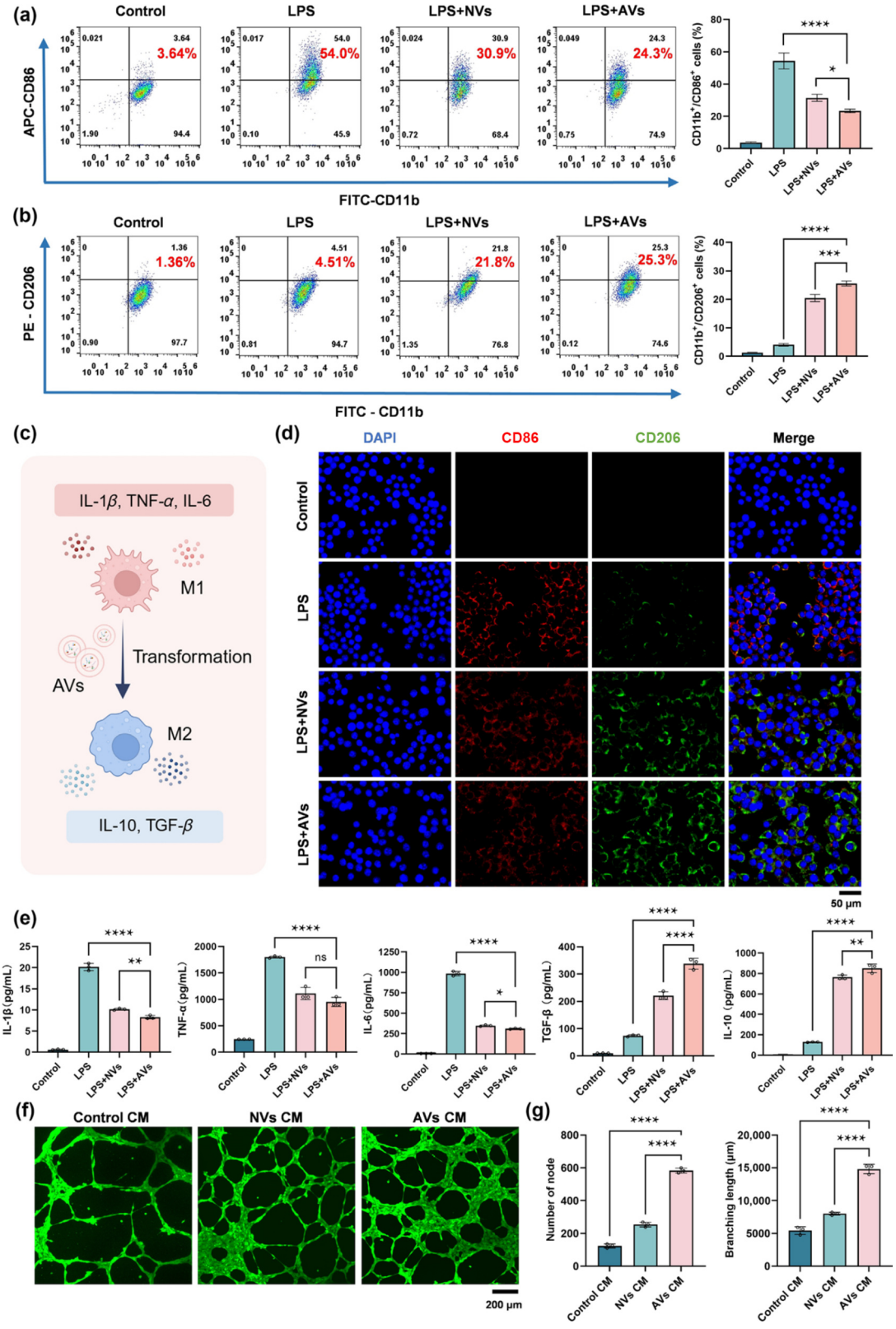

Figure 4 AVs reprogram macrophages toward an M2-like anti-inflammatory phenotype. Flow cytometry analysis of phenotypic changes of (a) CD86 and (b) CD206 in RAW264.7 macrophages. (c) Schematic illustration showing that AVs promote the transition of macrophages from the M1 to the M2 phenotype and enhance the secretion of anti-inflammatory cytokines such as IL-10 and TGF-*β*. (d) Immunofluorescence staining of RAW264.7 cells showing CD86 (red) and CD206 (green) expression, with DAPI used for nuclear staining. (e) ELISA analysis of pro-inflammatory cytokines (IL-1*β*, TNF-*α*, and IL-6) and anti-inflammatory cytokines (TGF-*β*, and IL-10), with quantitative statistics. (f) Representative fluorescence images of HUVEC tube formation and (g) corresponding quantitative analysis of the number of nodes and branching length following treatment with CM derived from different macrophage groups. Data are presented as mean ± SD ($n = 3$). $^{*}P < 0.05$; $^{**}P < 0.01$; $^{***}P < 0.001$; $^{****}P < 0.0001$.

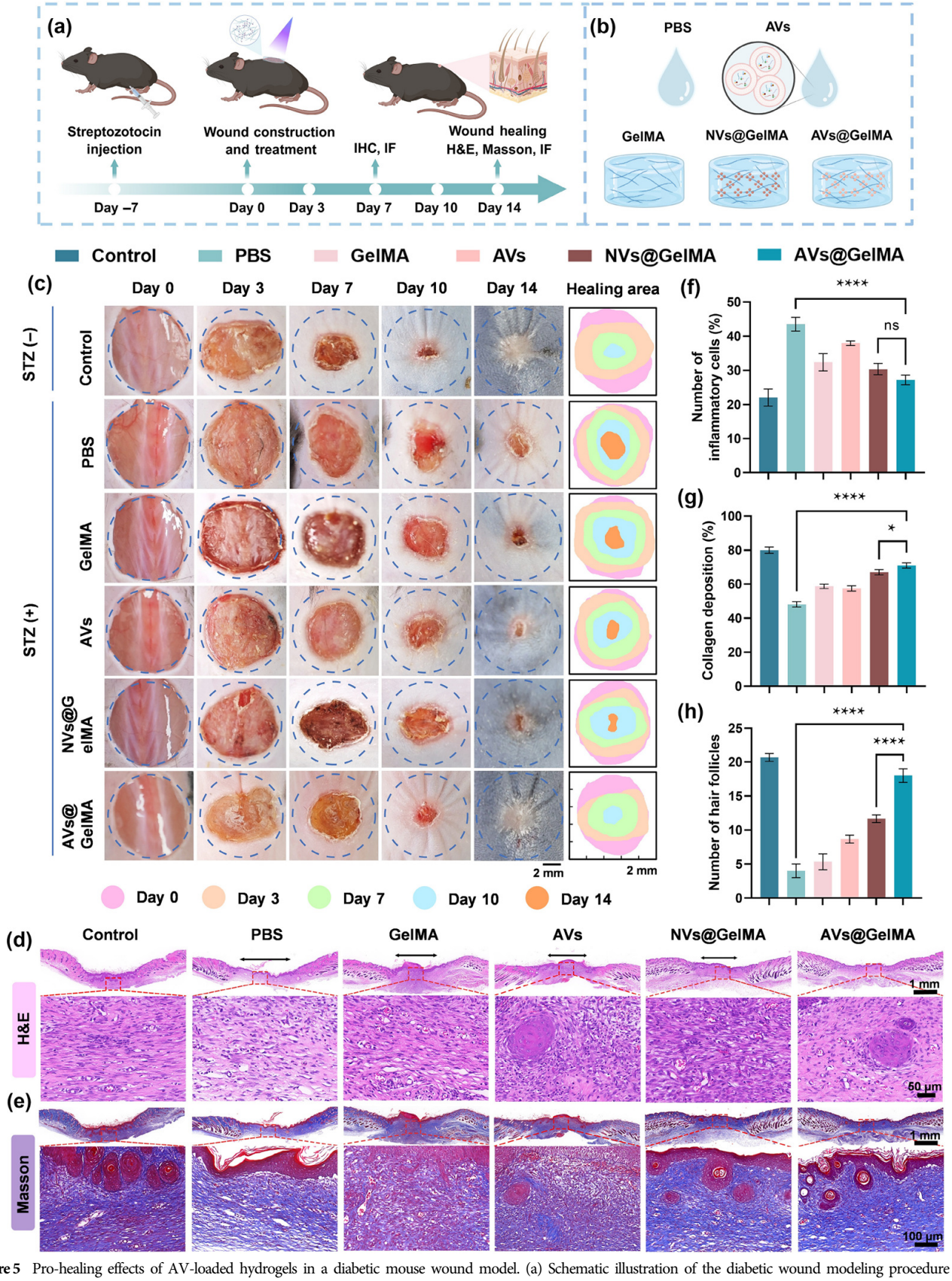

Figure 5 Pro-healing effects of AV-loaded hydrogels in a diabetic mouse wound model. (a) Schematic illustration of the diabetic wound modeling procedure and GelMA hydrogel-mediated vesicle delivery. (b) Diagram detailing the treatment regimens for each experimental group. (c) Representative gross images of wound closure across different groups on days 0, 3, 7, 10, and 14 (n = 5). (d) Representative H&E and (e) Masson's trichrome staining images of wound tissues collected on day 14. Quantitative histological analysis of (f) the inflammatory cell percentage, (g) collagen deposition area, and the (h) number of regenerated hair follicles across different groups. Data are presented as mean ± SD (n = 3, unless otherwise specified). *P < 0.05; **P < 0.01; ***P < 0.001; ****P < 0.0001.

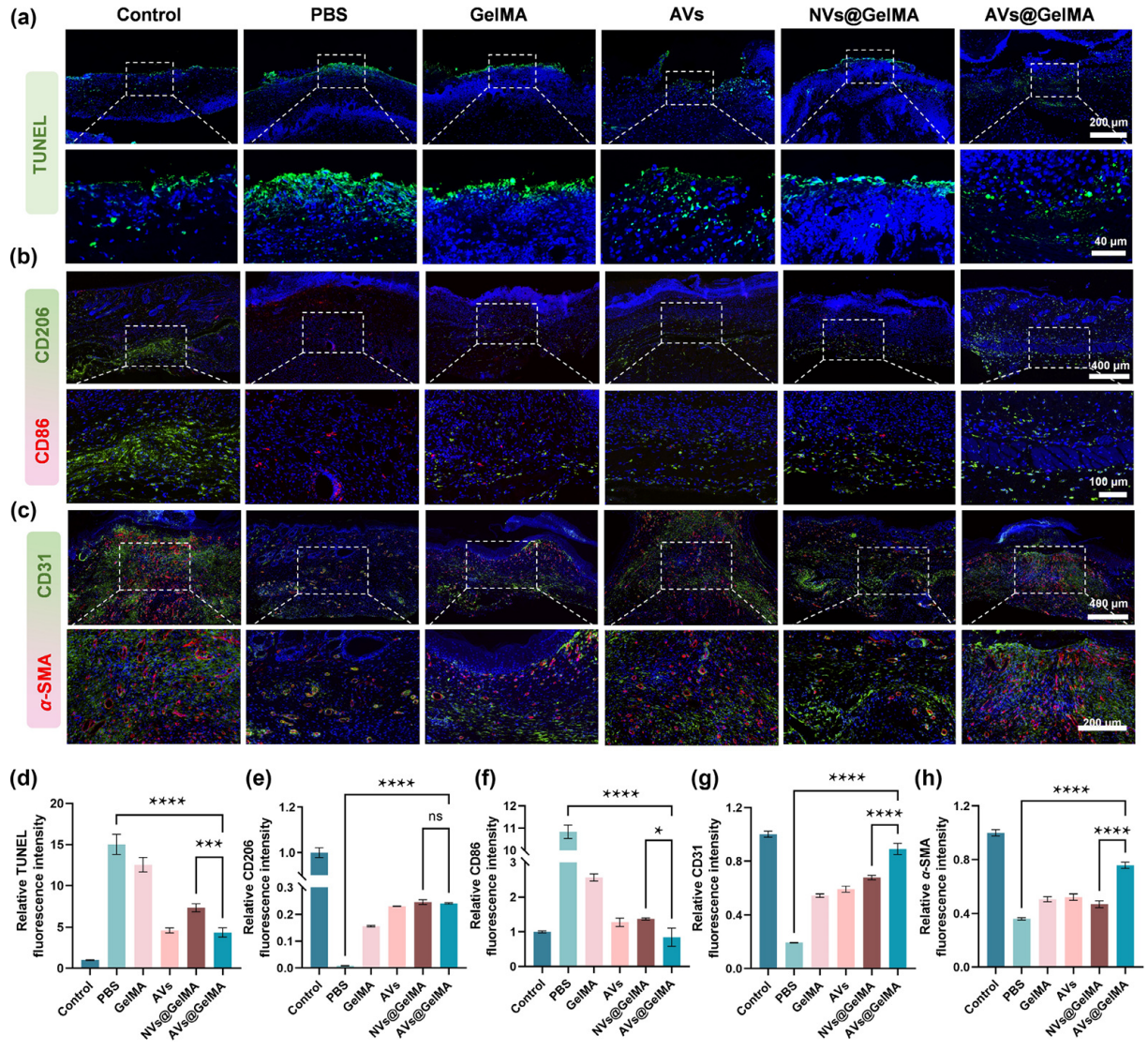

Figure 6 Spatiotemporal evaluation of apoptotic clearance, macrophage polarization, and angiogenesis in diabetic wounds. (a) Representative TUNEL staining at the early phase (day 3) to evaluate apoptotic cell accumulation. (b) Representative immunofluorescence double staining of CD206 (green, M2) and CD86 (red, M1) at the mid-phase (day 7) to assess macrophage polarization. (c) Representative immunofluorescence double staining of CD31 (green) and α-SMA (red) at the late remodeling phase (day 14) to evaluate neovascularization and vessel maturation. (d) Quantitative analysis of relative TUNEL fluorescence intensity. (e) Quantitative analysis of relative CD206 and (f) CD86 fluorescence intensity. (g) Quantitative analysis of relative CD31 and (h) α-SMA fluorescence intensity. Data are presented as mean ± SD (n = 3). *P < 0.05; **P < 0.01; ***P < 0.001; ****P < 0.0001.

maintained high CD206 expression (Fig. 6(e)) and most effectively restricted the pro-inflammatory CD86$^+$ M1 population (Fig. 6(f)). This targeted regulation highlights the capacity of AVs to rescue the hostile wound microenvironment from a chronic pro-inflammatory state. Ultimately, this resolved immune milieu translated into robust tissue regeneration. At day 14, CD31/α-SMA double staining (Fig. 6(c)) revealed that AVs@GelMA orchestrated a highly dense and mature vascular network. Quantitative analysis confirmed that both CD31$^+$ neovessel density and α-SMA$^+$ smooth muscle cell coverage were significantly higher in the AVs@GelMA group than in the NVs@GelMA and other controls (Figs. 6(g) and 6(h)). Collectively, these *in vivo* evaluations validate that AVs@GelMA accelerates wound healing through a tightly linked "efferocytosis-immunity-regeneration" cascade, effectively bridging early apoptotic clearance with profound macrophage reprogramming and late-stage mature angiogenesis.

3.7 AVs@GelMA accelerate diabetic wound healing by suppressing the NF-κB pathway

To further elucidate the potential mechanisms of AVs in chronic diabetic wound repair, we performed high-throughput RNA sequencing of wound tissues after 7 days of AVs@GelMA treatment and compared them with model controls. PCA demonstrated clear separation between the AVs@GelMA and control groups along PC1 (30.82%) and PC2 (22.11%) (Fig. S15 in the ESM), suggesting that this treatment strategy markedly remodeled the local transcriptional profile of wounds. Volcano plot analysis identified a total of 337 significantly differentially expressed genes (DEGs) (P < 0.05), including 80 upregulated and 257 downregulated genes (Fig. 7(a)). DEGs were visualized in a heatmap, showing systematic regulation of multiple gene expression patterns by AVs@GelMA intervention (Fig. 7(b)). To explore the biological relevance of these DEGs, Gene Ontology

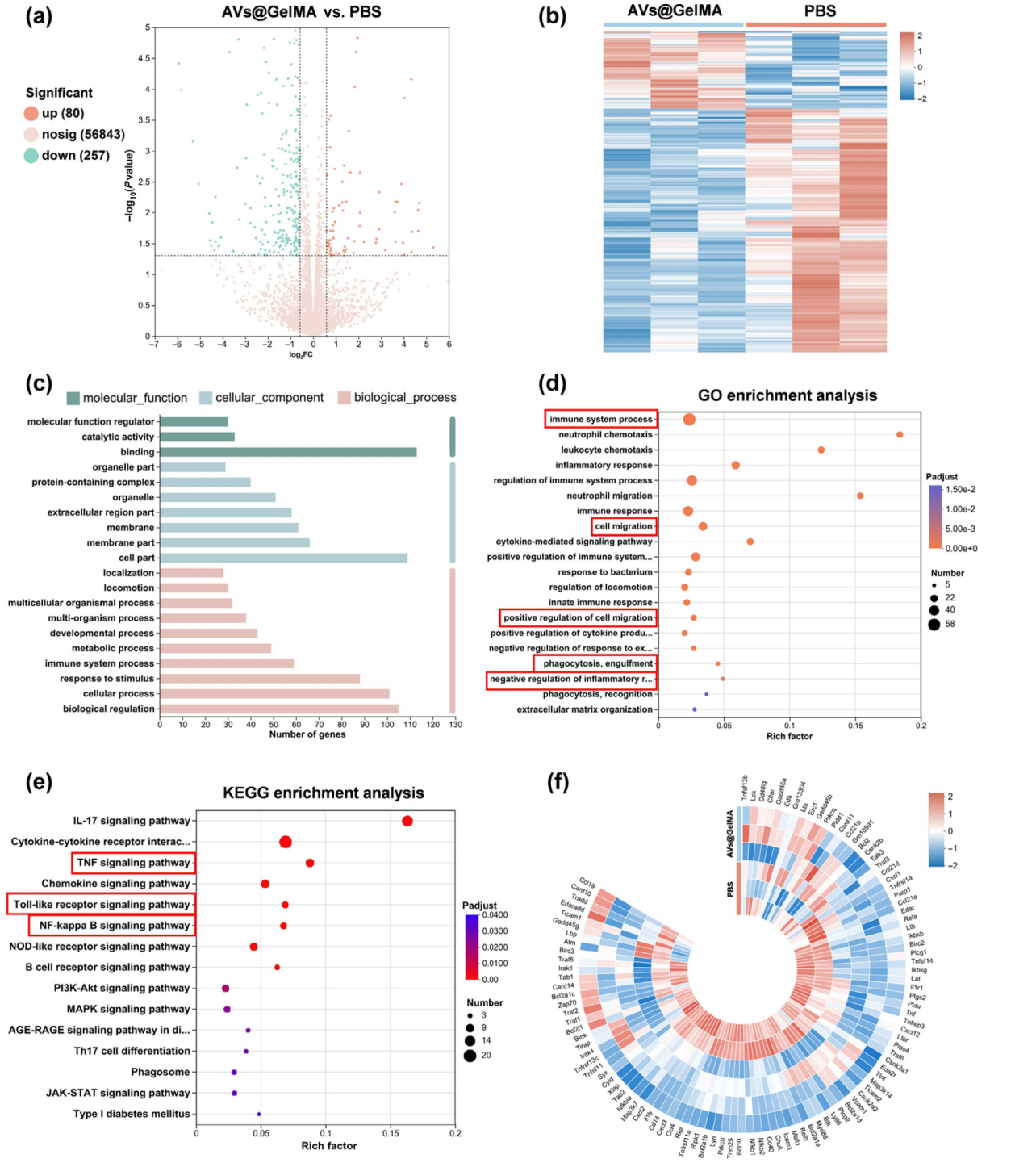

Figure 7 Transcriptomic analysis reveals potential mechanisms by which AVs@GelMA promote wound repair. (a) Volcano plot of DEGs in the AVs@GelMA group compared with the PBS group, with red indicating significantly upregulated genes and blue indicating downregulated genes. (b) Heatmap of DEGs showing differences in transcriptional expression patterns between the two groups. (c) GO functional annotation analysis. (d) GO enrichment analysis bubble plot of significantly enriched biological processes. (e) Kyoto Encyclopedia of Genes and Genomes (KEGG) pathway analysis showing enrichment of wound healing-related pathways. (f) Heatmap of NF-κB signaling pathway-related gene expression.

(GO) annotation was first performed. The results indicated that the DEGs were mainly involved in categories such as "biological regulation", "cellular process", "immune system process", "metabolic process", "membrane part", and "cell part" (Fig. 7(c)).

GO enrichment analysis further revealed significant enrichment of DEGs in biological processes closely related to wound healing, including immune regulation, inflammatory response, cell migration, and efferocytosis. Specifically, the GO terms "positive regulation of immune system process", "negative regulation of inflammatory response", and "positive regulation of cell migration" were significantly enriched ($P < 0.05$) (Fig. 7(d)). Notably, GO terms associated with macrophage phagocytic activity, such as

"phagocytosis, recognition" and "phagocytosis, engulfment", were also significantly enriched in the AVs@GelMA group, suggesting enhanced recognition and engulfment of apoptotic cells by macrophages. As a critical mechanism for the clearance of apoptotic and necrotic cells, efferocytosis plays a pivotal role in tissue repair by eliminating immune-stimulatory sources, attenuating inflammatory responses, and promoting tissue regeneration.

KEGG enrichment analysis of transcriptomic data showed that DEGs were significantly enriched in multiple signaling pathways closely associated with chronic inflammation, including the "NF-κB signaling pathway", "Toll-like receptor signaling pathway", and "TNF signaling pathway" (Fig. 7(e)). To further clarify changes in key pathways, we selected DEGs within the NF-κB pathway and generated a heatmap. The results revealed that several critical genes, including *RelA*, were downregulated in the AVs@GelMA group (Fig. 7(f)).

In addition, GSEA demonstrated that the "NF-κB signaling pathway", "TNF signaling pathway", and "Toll-like receptor signaling pathway" were all significantly negatively enriched in the AVs@GelMA group (Figs. 8(a)–8(c)). These findings suggest that AVs@GelMA exerts potent anti-inflammatory effects by suppressing these core inflammatory cascades. To verify this inhibitory trend at the tissue and protein levels, we performed immunohistochemical (IHC) staining. The results showed widespread expression of the NF-κB activation marker p-p65 and the pro-inflammatory cytokine TNF-α in the PBS group. Notably, AVs@GelMA treatment markedly reduced their expression to levels approaching those of the healthy control group, while concurrently significantly elevating the expression of the anti-inflammatory cytokine IL-10 (Figs. 8(e) and 8(g)). Furthermore, this robust anti-inflammatory response was corroborated by the significantly downregulated relative expression of pro-inflammatory cytokines (*TNF-α*, *IL-6*, and *IL-1β*) within the wound tissues (Fig. 8(h)). Moreover, GSEA also indicated a significant downregulation of the "apoptosis" pathway (Fig. 8(d)). To evaluate apoptotic cell accumulation within the wound bed, we performed TUNEL and caspase-3 immunofluorescence staining. The results demonstrated a marked reduction of apoptotic cells in both the AVs and AVs@GelMA groups, with AVs@GelMA exhibiting the most substantial clearance efficacy (Figs. 8(f), 8(i) and 8(j)). This suggests that AVs effectively reduce the accumulation of apoptotic cells in wounds, likely by enhancing macrophage efferocytosis, which is highly consistent with our earlier *in vitro* findings. By strengthening their capacity to engulf apoptotic cells, macrophages accelerate the resolution of inflammation. This process subsequently lays the foundation for polarization toward the M2 phenotype and the secretion of anti-inflammatory cytokines (such as IL-10), thereby establishing an immune microenvironment favorable for regenerative repair. Ultimately, this enhanced efferocytic activity provides a crucial prerequisite for inflammation resolution, angiogenesis, and subsequent tissue remodeling.

4 Conclusions

Integrating proteomic and functional analyses, we reveal that AVs are highly enriched in C1qbp. This key protein mediates the anchoring of C1q to apoptotic targets, thereby amplifying macrophage recognition and efferocytosis, an effect that is explicitly abrogated upon C1q blockade. Beyond apoptotic clearance, AVs actively stimulate cell proliferation and angiogenesis to orchestrate a pro-regenerative microenvironment. *In vivo*, topical application of AVs@GelMA markedly accelerated diabetic wound closure. This robust therapeutic efficacy was characterized by attenuated inflammatory infiltration, enhanced collagen deposition, extensive neovascularization, and a significant macrophage polarization toward the CD206-positive M2 phenotype. Mechanistically, AV-driven efferocytosis reprograms the wound bed toward a pro-resolving state while concurrently suppressing NF-κB inflammatory signaling and promoting reparative cellular migration. This synergistic cascade, conceptualized as an "efferocytosis-immunity-regeneration" tri-phasic process, effectively promotes the healing of chronic wounds. In summary, our mechanical extrusion strategy provides a highly scalable and reproducible platform for AV mass production that overcomes the bottlenecks of naturally secreted exosomes, while preserving excellent *in vivo* biosafety. Collectively, this study provides compelling, multi-faceted evidence supporting the translational potential of engineered AVs as precision immunomodulatory therapeutics for chronic wound management.

Electronic Supplementary Material: Supplementary material (additional data on vesicle engineering, cell-based assays, and *in vivo* wound healing) is available in the online version of this article at https://doi.org/10.26599/NR.2026.94908650.

Data availability

All data needed to support the conclusions in the paper are presented in the manuscript and the Electronic Supplementary Material (ESM). Additional data related to this paper may be requested from the corresponding author upon request.

Acknowledgements

This manuscript was supported by the National Natural Science Foundation of China (Nos. 82373274 and 82172706), Shanghai Municipal Health Commission (Nos. 202340267 and 2024ZZ1009), Shanghai Municipal Hospital Development Center (No. SHDC2023CRS020), and the Natural Science Foundation of the Department of Science and Technology of Hubei Province (No. 2025AFC086).

Declaration of competing interest

All the contributing authors report no conflict of interests in this work.

Author contribution statement

L. D.: Conceptualization, data curation, investigation, writing – original draft, validation, visualization. T. R. Z.: Conceptualization, writing – original draft, investigation, formal analysis, methodology. Y. X. P.: Conceptualization, data curation, methodology, writing – original draft. J. L.: Investigation, methodology, formal analysis. J. Y. L.: Investigation, visualization, methodology. X. Y. Z.: Methodology. T. Y. M.: Methodology. D. H. L.: Visualization. Z. C.: Visualization, funding acquisition. Y. G.: Data curation, funding acquisition. Q. G. Z.: Conceptualization, supervision, writing – review & editing, funding acquisition. Z. G. T.: Conceptualization, supervision, writing – review & editing, funding acquisition. Z. J. C.: Conceptualization, supervision, writing – review & editing, funding acquisition.

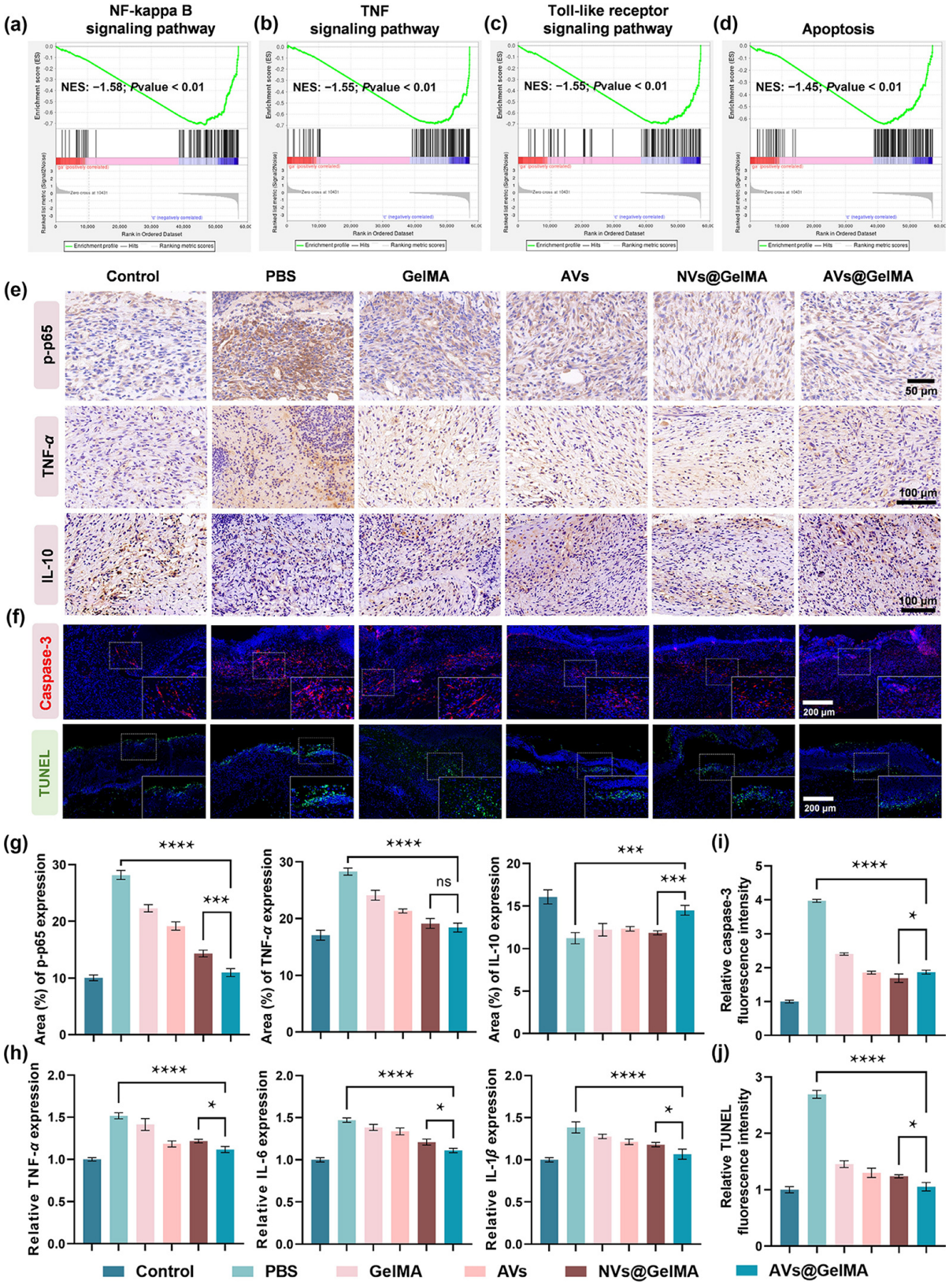

Figure 8 AVs@GelMA hydrogels inhibit NF-κB signaling, resolve inflammation, and reduce apoptotic cell accumulation in diabetic wounds. Gene set enrichment analysis (GSEA) enrichment analysis of the (a) NF-κB, (b) TNF, and (c) Toll-like receptor signaling pathways. (d) GSEA enrichment analysis of the apoptosis pathway. (e) Representative immunohistochemical staining images of p-p65, TNF-α, and IL-10 in wound tissues on day 7. (f) Representative immunofluorescence staining images of caspase-3 and TUNEL in wound tissues on day 7. (g) Quantitative analysis of the positive area percentages for p-p65, TNF-α, and IL-10 based on the IHC images. (h) Relative expression levels of pro-inflammatory cytokines (TNF-α, IL-6, and IL-1β) in wound tissues. (i) Quantitative analysis of relative fluorescence intensities for caspase-3 and (j) TUNEL. Data are presented as mean ± SD ($n = 3$). *$P < 0.05$; **$P < 0.01$; ***$P < 0.001$; ****$P < 0.0001$.

Informed consent

Not applicable.

Ethics statement

Animal studies were approved by the Ethics Committee of Shanghai Skin Disease Hospital, Shanghai, China (approval ID: 2021-91).

Use of AI statement

None.

References

[1] Xu, Y.; Lu, J. L.; Li, M.; Wang, T. G.; Wang, K.; Cao, Q. Y.; Ding, Y.; Xiang, Y.; Wang, S. Y.; Yang, Q. Q. et al. Diabetes in China part 1: Epidemiology and risk factors. *Lancet Public Health* **2024**, *9*, e1089–e1097.

[2] Jia, W. P.; Chan, J. C.; Wong, T. Y.; Fisher, E. B. Diabetes in China: Epidemiology, pathophysiology and multi-omics. *Nat. Metab.* **2025**, *7*, 16–34.

[3] Sun, H.; Saeedi, P.; Karuranga, S.; Pinkepank, M.; Ogurtsova, K.; Duncan, B. B.; Stein, C.; Basit, A.; Chan, J. C. N.; Mbanya, J. C. et al. IDF Diabetes Atlas: Global, regional and country-level diabetes prevalence estimates for 2021 and projections for 2045. *Diabetes Res. Clin. Pract.* **2022**, *183*, 109119.

[4] Shi, S. P.; Yang, P. Y.; Liu, X. Z.; Li, Y. J.; Yang, C. Evidence mapping of clinical practice guideline recommendations for self-management strategies of diabetic foot ulcers. *Adv. Wound Care*, in press, DOI: 10.1089/wound.2024.0276.

[5] Zhou, Y. M.; Jia, W. B.; Bi, J. X.; Liu, M.; Liu, L. L.; Zhou, H.; Gu, G. F.; Chen, Z. G. Sulfated hyaluronic acid/collagen-based biomimetic hybrid nanofiber skin for diabetic wound healing: Development and preliminary evaluation. *Carbohydr. Polym.* **2024**, *334*, 122025.

[6] Liu, C. N.; Ponsero, A. J.; Armstrong, D. G.; Lipsky, B. A.; Hurwitz, B. L. The dynamic wound microbiome. *BMC Med.* **2020**, *18*, 358.

[7] Armstrong, D. G.; Tan, T. W.; Boulton, A. J. M.; Bus, S. A. Diabetic foot ulcers: A review. *JAMA* **2023**, *330*, 62–75.

[8] NCD Risk Factor Collaboration (NCD-RisC). Worldwide trends in diabetes prevalence and treatment from 1990 to 2022: A pooled analysis of 1108 population-representative studies with 141 million participants. *Lancet* **2024**, *404*, 2077–2093.

[9] Xiong, Y.; Feng, Q.; Lu, L.; Zha, K.; Yu, T.; Lin, Z.; Hu, Y. Q.; Panayi, A. C.; Nosrati-Ziahmagi, V.; Chu, X. Y. et al. Immunomodulatory hydrogels: Advanced regenerative tools for diabetic foot ulcer. *Adv. Funct. Mater.* **2023**, *33*, 2213066.

[10] Zheng, Z. W.; Yang, J.; Zheng, W.; Chu, Z. Y.; Wang, W. N.; Qian, H. S.; Xu, L. L. Comprehensive management of diabetic ulceration: Strategies and perspectives. *J. Control. Release* **2025**, *385*, 114058.

[11] He, X. Y.; Gao, Y. C.; Wang, X.; Zhang, C. K.; Xia, Z. X.; Xu, W.; Yang, H.; Tao, G.; Cai, R.; Chen, J. L. et al. Dual-network hydrogel loaded with antler stem cells conditioned medium and EGCG promotes diabetic wound healing through antibacterial, antioxidant, anti-inflammatory, and angiogenesis. *Mater. Today Bio* **2025**, *31*, 101612.

[12] Cong, R.; Deng, C. Y.; Li, P. W.; Tang, Y. W.; Hou, J. F.; Zhao, J. H.; Wang, Q. L.; Chen, Y. Y.; Tu, J. S.; Jiang, X. Q. et al. Dimeric copper peptide incorporated hydrogel for promoting diabetic wound healing. *Nat. Commun.* **2025**, *16*, 5797.

[13] Li, X. Y.; Yi, M.; Song, Z. Y.; Ni, T. Y.; Tu, L. Y.; Yu, M.; Zhang, L. T.; Shi, J. P.; Gao, W. C.; Zhang, Q. et al. A calcitonin gene-related peptide co-crosslinked hydrogel promotes diabetic wound healing by regulating M2 macrophage polarization and angiogenesis. *Acta Biomater.* **2025**, *196*, 109–122.

[14] Doran, A. C.; Yurdagul, A. Jr. ; Tabas, I. Efferocytosis in health and disease. *Nat. Rev. Immunol.* **2020**, *20*, 254–267.

[15] Xiao, L. J.; Zhang, L. Q.; Guo, C. L.; Xin, Q. L.; Gu, X. S.; Jiang, C. P.; Wu, J. H. "Find Me" and "Eat Me" signals: Tools to drive phagocytic processes for modulating antitumor immunity. *Cancer Commun.* **2024**, *44*, 791–832.

[16] Chen, S. J.; Zhang, H. J.; Wang, Z. H.; Zhu, D. X.; Li, Y. H.; Zhang, Y. Z.; Wang, D. X.; Chen, S. W.; Liu, H.; Kang, X. W. Macrophage efferocytosis as a therapeutic strategy in intervertebral disc degeneration. *Cell Prolif.* **2025**, *58*, e70068.

[17] Li, B.; Xin, Z. L.; Gao, S. Y.; Li, Y. J.; Guo, S. S.; Fu, Y.; Xu, R. Y.; Wang, D. M.; Cheng, J.; Liu, L. K. et al. SIRT6-regulated macrophage efferocytosis epigenetically controls inflammation resolution of diabetic periodontitis. *Theranostics* **2023**, *13*, 231–249.

[18] Boada-Romero, E.; Martinez, J.; Heckmann, B. L.; Green, D. R. The clearance of dead cells by efferocytosis. *Nat. Rev. Mol. Cell Biol.* **2020**, *21*, 398–414.

[19] Xie, Y. L.; Yang, J. M.; Zhu, H.; Yang, R. Y.; Fan, Y. L. The efferocytosis dilemma: How neutrophil extracellular traps and PI3K/Rac1 complicate diabetic wound healing. *Cell Commun. Signal.* **2025**, *23*, 103.

[20] Ge, Y.; Huang, M.; Yao, Y. M. Efferocytosis and its role in inflammatory disorders. *Front. Cell Dev. Biol.* **2022**, *10*, 839248.

[21] Li, Y. Z.; Li, P. Y.; Song, J. Y.; Zhang, X.; Xiao, H. T.; Wang, R.; Duan, Z. Y.; Luo, K.; Xu, X. W. Targeting efferocytosis for tissue regeneration: From microenvironment reprogramming to clinical translation. *Theranostics* **2026**, *16*, 3697–3734.

[22] Gong, T.; Liu, L.; Jiang, W.; Zhou, R. B. DAMP-sensing receptors in sterile inflammation and inflammatory diseases. *Nat. Rev. Immunol.* **2020**, *20*, 95–112.

[23] Ma, M.; Jiang, W.; Zhou, R. B. DAMPs and DAMP-sensing receptors in inflammation and diseases. *Immunity* **2024**, *57*, 752–771.

[24] Zhang, Y. Q.; Nie, R.; Feng, Z. Y.; Fan, M. H.; Shen, Z. X.; Zhang, X. Z.; Zhang, Q. Y.; Zou, C. Y.; Zhang, J. Y.; Huang, K. et al. Efferocytosis in tissue engineering: A comprehensive review of emerging therapeutic strategies for enhanced tissue repair and regeneration. *Bioact. Mater.* **2025**, *52*, 155–181.

[25] Wang, R. Y.; Gu, S.; Kim, Y. H.; Lee, A.; Lin, H. D.; Jiang, D. S. Diabetic wound repair: From mechanism to therapeutic opportunities. *MedComm* **2025**, *6*, e70406.

[26] Choudhury, S.; Dhoke, N. R.; Chawla, S.; Das, A. Bioengineered MSC^{Cxcr2} transdifferentiated keratinocyte-like cell-derived organoid potentiates skin regeneration through ERK1/2 and STAT3 signaling in diabetic wound. *Cell. Mol. Life Sci.* **2024**, *81*, 172.

[27] Jaraba-Álvarez, W. V.; Uscanga-Palomeque, A. C.; Sanchez-Giraldo, V.; Madrid, C.; Ortega-Arellano, H.; Halpert, K.; Quintero-Gil, C. Hypoxia-induced metabolic reprogramming in mesenchymal stem cells: Unlocking the regenerative potential of secreted factors. *Front. Cell Dev. Biol.* **2025**, *13*, 1609082.

[28] Li, M. J.; Tang, Q.; Liao, C. C.; Wang, Z.; Zhang, S. Y.; Liang, Q. Q.; Liang, C.; Liu, X. D.; Zhang, J. Y.; Tian, W. D. et al. Extracellular vesicles from apoptotic BMSCs ameliorate osteoporosis via transporting regenerative signals. *Theranostics* **2024**, *14*, 3583–3602.

[29] He, X. M.; Hong, W. Q.; Yang, J. Y.; Lei, H.; Lu, T. Q.; He, C.; Bi, Z. F.; Pan, X. Y.; Liu, Y.; Dai, L. Z. et al. Spontaneous apoptosis of cells in therapeutic stem cell preparation exert immunomodulatory effects through release of phosphatidylserine. *Signal Transduct. Target. Ther.* **2021**, *6*, 270.

[30] Pang, S. H. M.; D'Rozario, J.; Mendonca, S.; Bhuvan, T.; Payne, N. L.; Zheng, D.; Hisana, A.; Wallis, G.; Barugahare, A.; Powell, D. et al. Mesenchymal stromal cell apoptosis is required for their therapeutic function. *Nat. Commun.* **2021**, *12*, 6495.

[31] Wang, F.; Li, L. Y.; Deng, J. Y.; Mo, S. S.; Ai, J. C.; Xiao, Y. X.; Li, Q. S.; Ding, D. D.; Zhang, Y. X.; Zhou, D. F. et al. Extruded

nanovesicles derived from umbilical cord mesenchymal stem cells exhibit No tumorigenic potential. *Bioact. Mater.* **2025**, *52*, 866–876.
[32] Xu, X.; Xu, L. M.; Wang, J. Z.; Wen, C. N.; Xia, J.; Zhang, Y. M.; Liang, Y. J. Bioinspired cellular membrane-derived vesicles for mRNA delivery. *Theranostics* **2024**, *14*, 3246–3266.
[33] Frey, L.; Ziętara, N.; Łyszkiewicz, M.; Marquardt, B.; Mizoguchi, Y.; Linder, M. I.; Liu, Y. S.; Giesert, F.; Wurst, W.; Dahlhoff, M. et al. Mammalian VPS45 orchestrates trafficking through the endosomal system. *Blood* **2021**, *137*, 1932–1944.
[34] Lu, N.; Shen, Q.; Mahoney, T. R.; Liu, X. H.; Zhou, Z. Three sorting nexins drive the degradation of apoptotic cells in response to PtdIns(3)P signaling. *Mol. Biol. Cell* **2011**, *22*, 354–374.
[35] Sachet, M.; Liang, Y. Y.; Oehler, R. The immune response to secondary necrotic cells. *Apoptosis* **2017**, *22*, 1189–1204.
[36] Mochizuki, T.; Kojima, Y.; Nishiwaki, Y.; Harakuni, T.; Masai, I. Endocytic trafficking factor VPS45 is essential for spatial regulation of lens fiber differentiation in zebrafish. *Development* **2018**, *145*, dev170282.
[37] Donat, C.; Thanei, S.; Trendelenburg, M. Binding of von willebrand factor to complement C1q decreases the phagocytosis of cholesterol crystals and subsequent IL-1 secretion in macrophages. *Front. Immunol.* **2019**, *10*, 2712.
[38] Gao, L.; Manaenko, A.; Zeng, F.; Li, J. C.; Liu, L. L.; Xie, R. C.; Zhang, X. H.; Zhang, J. H.; Mei, Q. Y.; Tang, J. P. et al. Efferocytosis: A new therapeutic target for stroke. *Chin. Med. J.* **2024**, *137*, 2843–2850.
[39] Xu, Y. D.; Liang, X. C.; Li, Z. P.; Wu, Z. S.; Yang, J.; Jia, S. Z.; Peng, R.; Li, Z. Y.; Wang, X. H.; Luo, F. J. et al. Apoptotic body-inspired nanotherapeutics efficiently attenuate osteoarthritis by targeting BRD4-regulated synovial macrophage polarization. *Biomaterials* **2024**, *306*, 122483.